A new family of solutions of the force free field equation

E.A. Evangelidis (eevangel@env.duth.gr)
Dept. of Environmental Eng., Lab. of Non–Conventional Sources of Energy, Demokritos University of Thrace, Kimeria, 67100 Xanthi, Greece

G.J.J. Botha (gert@math.ucl.ac.uk)
Mathematics Dept., University College London, Gower Street, London WC1E 6BT, UK

Abstract. A new family of solutions has been found for force free magnetic fields and Beltrami flows, which admits a complete classification in terms of the eigenvalues of the problem. In the absence of boundary values to determine them uniquely, the eigenvalues correspond to the entire set of real numbers, except for zero. The eigenvalues are degenerate in that each eigenvalue has many eigensolutions associated with it. For each eigensolution we have been able to identify sets of equilibrium or null points and lines. The linear mappings of these null points and lines are all unstable. Finally, we derive the first integral of energy associated with this family of solutions.

1. Introduction

It is well known that the force free field equation

$$\mathbf{B} \wedge \nabla \wedge \mathbf{B} = 0 \tag{1}$$

admits the solution given by Arnold (1965), which in its most general form can be written as

$$\begin{aligned} B_x &= A\sin(nz) + C\cos(ny), \\ B_y &= B\sin(nx) + A\cos(nz), \\ B_z &= C\sin(ny) + B\cos(nx). \end{aligned} \tag{2}$$

The subsequent publication by Hénon (1966) corroborated numerically the theoretical predictions made by Arnold in the former paper, namely that the Beltrami sub-Eulerian flow formally characterized by Eq. (1), is ergodic. The importance of this type of fields in hydrodynamics (where $\mathbf{B}$ is a velocity field) and magnetohydrodynamics (where $\mathbf{B}$ is a magnetic field) can hardly be overemphasized, since in both cases energy and mass can be transported with no dissipation of energy and released at the null points of the flow. As such, linear force free fields have been used to describe phenomena in the solar photosphere (Moon et al., 2002), the solar corona (Bungey et al., 1996; Démoulin et al., 1997; Berton, 2000; Yurchyshyn et al., 2000), as well as astrophysical and laboratory plasmas (Clegg et al., 2000).

Eq. (1) can be written as an eigenvalue equation

$$\nabla \wedge \mathbf{B} = \alpha \mathbf{B}, \tag{3}$$

with the scalar quantity α a constant of proportionality, when provided with suitable boundary values. Arnold's solution is an eigensolution for $\alpha = n$. For the last forty years this solution has been the only known solution in three-dimensional Cartesian space for constant α (i.e. linear force free fields), and as such it has provided valuable insight into the nature of these strange fields (Biskamp, 1993; Marsh, 1996). It is known that Arnold's solution has eight hyperbolic equilibrium points associated with every energy level (when $n = 1$), as well as ergodic and non-ergodic regimes in phase space (Dombre et al., 1986), which can be determined through its first integral of energy (Evangelidis et al., 2000). The elegance of Arnold's solution has made it a convenient tool to study coronal activity in the sun (Galsgaard and Nordlund, 1997; Galsgaard et al., 2000). Naturally, one would like to know whether there are any other solutions. We have been able to construct a family of solutions, of which the Arnold solution is not a member. The first integral of energy for this new family of solutions is also presented. In anticipation of the detailed exposition, we mention that each energy manifold is characterized by the existence of equilibrium or null points, as well as equilibrium lines parallel to one of the Cartesian axes.

2. The solution

Let us consider the magnetic field $\mathbf{B}$, with components

$$B_x = \int A_{lmn} \frac{(m^2+n^2)}{k} \cos(lx)\cos(my)\cos(nz)\,\delta_{lmn}\,dl\,dm\,dn, \tag{4}$$

$$B_y = -\int A_{lmn} \left[n\cos(lx)\cos(my)\sin(nz) - \frac{lm}{k}\sin(lx)\sin(my)\cos(nz) \right] \delta_{lmn}\,dl\,dm\,dn, \tag{5}$$

$$B_z = \int A_{lmn} \left[m\cos(lx)\sin(my)\cos(nz) + \frac{ln}{k}\sin(lx)\cos(my)\sin(nz) \right] \delta_{lmn}\,dl\,dm\,dn, \tag{6}$$

where the integration is over the real numbers l, m, and n, subject to the constraint imposed by the Dirac-delta function, which is defined as $\delta_{lmn} = \delta_{lmn}(l^2+m^2+n^2-k^2)$. It is easily verified by direct substitution,

that this magnetic field is divergence free and satisfies Eq. (3) for $\alpha = k$. It is noted that the eigenvalue k is triply degenerate in that an infinite set of values of l, m, and n corresponds to a single eigenvalue k. One way to visualize this is by constructing eigenspheres of radius k for different values of l, m, and n. This is in stark contrast to Arnold's solution (Eqs. 2), where the n inside the argument of the trigonometric functions determines the constant α in Eq. (3) uniquely. The above solution is not related to Arnold's solution, in that one cannot reproduce one solution from the other by any choice of parameters. Lastly, whereas Eq. (2) has three arbitrary constants (A, B, and C), the new solution has only one in front of the terms for every particular combination of l, m, and n, namely A_{lmn}.

3. Integral of energy

In order to construct the integral of energy, we follow the method expounded in our previous publication (Evangelidis et al., 2000). From the expressions

$$\frac{dx_i}{ds} = B_{x_i}, \tag{7}$$

$$\frac{d^2x_i}{ds^2} = \frac{\partial B_{x_i}}{\partial x_j} B_{x_j}, \tag{8}$$

where x_i and $x_j \in \{x, y, z\}$, we find

$$\frac{d^2x}{ds^2} = -Jl\sin(2lx)\left[L + n^2\cos(2my) + m^2\cos(2nz)\right], \tag{9}$$

$$\frac{d^2y}{ds^2} = Jm\sin(2my)\left[M - n^2\cos(2lx) + l^2\cos(2nz)\right], \tag{10}$$

$$\frac{d^2z}{ds^2} = Jn\sin(2nz)\left[N - m^2\cos(2lx) + l^2\cos(2my)\right], \tag{11}$$

where the constants J, L, M, and N are defined by

$$L = m^2 + n^2, \qquad M = \frac{l^2m^2 - k^2n^2}{L}, \tag{12}$$

$$J = A_{lmn}^2\frac{L}{4k^2}, \qquad N = \frac{l^2n^2 - k^2m^2}{L}, \tag{13}$$

and $k^2 = l^2 + m^2 + n^2$ as before. In these expressions we have omitted the integral representation by means of the Dirac-delta function, so that we do not overburden the notation. These results can be written

in the succinct form

$$\frac{d^2x_i}{ds^2} = -\frac{\partial U}{\partial x_i}, \tag{14}$$

with x_i representing x, y, and z, and the potential U given by

$$\begin{aligned} U \;=\; -\frac{J}{2}\,[&L\cos(2lx) - M\cos(2my) - N\cos(2nz) \\ &-l^2\cos(2my)\cos(2nz) + m^2\cos(2lx)\cos(2nz) \\ &+n^2\cos(2lx)\cos(2my)\big]\,. \end{aligned} \tag{15}$$

The existence of a potential function allows for the derivation of the Hamiltonian of the family of solutions, namely

$$H = \frac{1}{2}\left(\dot{x}^2 + \dot{y}^2 + \dot{z}^2\right) + U. \tag{16}$$

This expression is also the formulation for the first integral of energy, i.e. $E = H$, or more explicitly,

$$\begin{aligned} E \;=\; F\,[\,&\cos(2lx)\cos(2my)\cos(2nz) \\ &+ \cos(2lx)\cos(2my) + \cos(2lx)\cos(2nz) + \cos(2my)\cos(2nz) \\ &+ \cos(2lx) + \cos(2my) + \cos(2nz) + G\,] \end{aligned} \tag{17}$$

with the constants F and G given by

$$F \;=\; A_{lmn}^2\frac{(m^2+n^2)(1-m^2-n^2)}{16k^2}, \tag{18}$$

$$G \;=\; \frac{1+k^2+l^2}{1-k^2+l^2}. \tag{19}$$

4. Null points and lines

At the equilibrium or null points the solution becomes $B_x = B_y = B_z = 0$. From Eq. (4) it follows that $B_x = 0$ when one of the following is true:

$$\cos(lx) \;=\; 0, \tag{20}$$

$$\cos(my) \;=\; 0, \tag{21}$$

$$\cos(nz) \;=\; 0. \tag{22}$$

From Eq. (5) we observe that for B_y to be zero under (20), either $\sin(my)$ or $\cos(nz)$ should be zero. In the former case Eq. (6) dictates that $B_z = 0$ only when $\sin(nz) = 0$, while in the latter case $B_z = 0$ only

when $\cos(my) = 0$. Collecting these results, we obtain the following sets of equilibrium points:

$$[\ \cos(lx) = 0\ ;\ \sin(my) = 0\ ;\ \sin(nz) = 0\ ], \tag{23}$$

$$[\ \cos(lx) = 0\ ;\ \cos(my) = 0\ ;\ \cos(nz) = 0\ ]. \tag{24}$$

A similar analysis with condition (21) produces the null points of B_y when $\sin(lx) = 0$ or $\cos(nz) = 0$. These, combined with the null points of B_z, produce equilibrium points that are described by

$$[\ \sin(lx) = 0\ ;\ \cos(my) = 0\ ;\ \cos(nz) = 0\ ], \tag{25}$$

as well as equilibrium lines that are parallel to the Ox axis, each of which satisfies the equation

$$[\ x\ ;\ \cos(my) = 0\ ;\ \cos(nz) = 0\ ] \tag{26}$$

for all values of x. Finally, condition (22) duplicates the results already obtained, and does not introduce any new information.

A comparison of the null points (24) and (25) with the description of the null lines (26), shows that all these points lie on the lines. It follows that the solution contains the null points (23) and the null lines (26). We can rewrite these as

$$\left[\ \frac{(2i+1)\pi}{2l}\ ;\ \frac{\pi j}{m}\ ;\ \frac{\pi h}{n}\ \right], \tag{27}$$

$$\left[\ x\ ;\ \frac{(2f+1)\pi}{2m}\ ;\ \frac{(2g+1)\pi}{2n}\ \right], \tag{28}$$

where $f, g, h, i, j \in \{0, 1, 2, ...\}$. As the values of l, m, and n increase, the distances between the null points and null lines decrease, so that more points and lines fit into the interval $[0, 2\pi]$. In the case of l, m, and n integers, we obtain discrete sets of null points, while for non-integers the null points fill the whole of the interval $[0, 2\pi]$.

When $l = 0$, the null points disappear and we are left with the null lines parallel to the Ox axis. To see this, we substitute the $l = 0$ into the solution (4) to (6) to obtain

$$B_x = \int A_{0mn}\sqrt{m^2+n^2}\cos(my)\cos(nz)\,\delta_{0mn}\,dm\,dn, \tag{29}$$

$$B_y = -\int A_{0mn}n\cos(my)\sin(nz)\,\delta_{0mn}\,dm\,dn, \tag{30}$$

$$B_z = \int A_{0mn}m\sin(my)\cos(nz)\,\delta_{0mn}\,dm\,dn, \tag{31}$$

for all values of x. It follows that we have null lines parallel to the Ox axis, and it is easy to verify that they are described by the points (26), or more explicitly by (28). In a similar way, we find that for $m = 0$ we have null lines running parallel to the Oy axis, and for $n = 0$ we have null lines running parallel to the Oz axis. When two of the three constants l, m, n are zero, we obtain either the trivial case, or a magnetic field reduced to two dimensions with no null points or lines.

In order to visualize the structure of the magnetic field, we reduce the complexity of the field by choosing a single term from the general solution (4) to (6), namely $A_{111} = l = m = n = 1$. Figs. 1 and 2 are respectively contour and vector plots of the magnetic field $\mathbf{B}$ on the (y, z) plane, presented at constant x values ($x = 0$, $\pi/2$, π, and $3\pi/2$). This field has four null lines parallel to Ox, situated on the (y, z) plane at $(i\pi/2, j\pi/2)$, with $i, j \in \{1, 3\}$. They are clearly visible in Fig. 1(a) as the four minima of the contour plot. As well as these null lines, the solution with $A_{111} = l = m = n = 1$ has eight null points, situated at $((2h + 1)\pi/2, i\pi, j\pi)$, with $h, i, j \in \{0, 1\}$. Four of these null points, together with the four null lines, are shown in Fig. 1(b). Both the y and z directions are periodic. This means that the magnetic field structure around the null point at $(\pi/2, \pi, 0)$ continues at $z = 2\pi$, and the structure around $(\pi/2, 0, \pi)$ continues at $y = 2\pi$. The null point $(\pi/2, 0, 0)$ lies at the corner of the contour plot, so that the magnetic field structure around it is divided into four parts, each of which is situated at $(y, z) = (0, 0)$, $(0, 2\pi)$, $(2\pi, 0)$, and $(2\pi, 2\pi)$. Due to the presence of the four null points and the four null lines at $x = \pi/2$, the maximum value of the magnetic field is half of what it is at $x = 0$, where only the four null lines are present. Fig. 1(d) shows the other four null points of solution $A_{111} = l = m = n = 1$ at $x = 3\pi/2$.

Figs. 3 and 4 present contour and vector plots of the (x, z) plane at specific values of y. Four of the eight null points are situated at $y = 0$, and the other four are at $y = \pi$. Fig. 3(a) shows the four null points at $((2i + 1)\pi/2, 0, j\pi)$, with $i, j \in \{0, 1\}$. The (x, z) plane is periodic in both directions, so that the magnetic field structure around the two null points at $(\pi/2, 0, 0)$ and $(3\pi/2, 0, 0)$ continues at $z = 2\pi$. The other four null points lie at $y = \pi$, as shown in Fig. 3(c). Two of the four null lines parallel to the Ox axis are situated at $y = \pi/2$ and two are situated at $y = 3\pi/2$. In the Oy direction the null lines are situated midway between the planes with null points, so that the (x, z) planes containing the lines, contain no null points. Figs. 3(b) and (d) show the lines at $z = \pi/2$ and $z = 3\pi/2$. The local maxima on these (x, z) planes are caused by the null points lying at $y = 0$ and $y = \pi$.

By choosing the z planes 0, $\pi/2$, π, and $3\pi/2$, a similar picture emerges as in Figs. 3 and 4. The only difference is that the z axis is replaced with the y axis to form (x, y) planes.

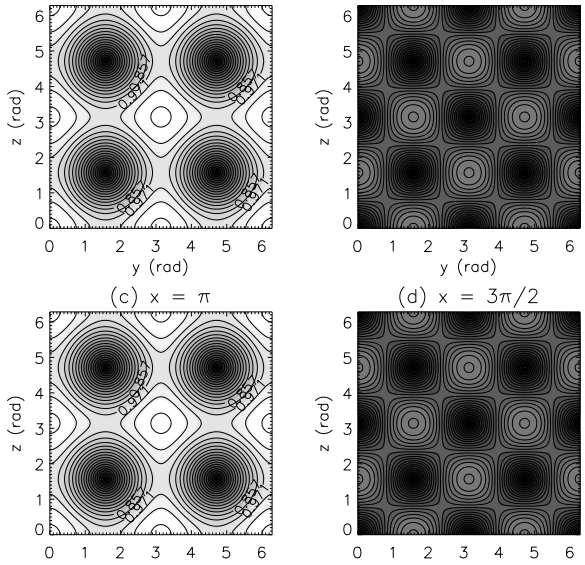

Figure 1. Contour plot of the field magnitude B on the (y, z) plane for solution with $A_{111} = l = m = n = 1$. Colour scale: white represents the maximum value 1.15 and black represents zero.

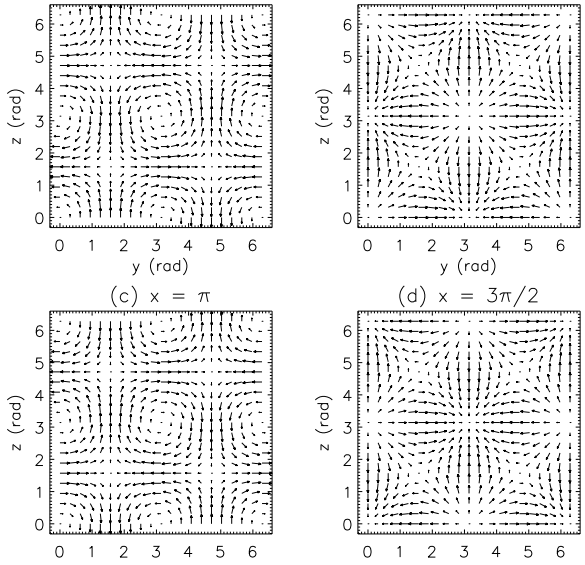

Figure 2. Vector plot of B on the (y, z) plane for solution with $A_{111} = l = m = n = 1$. The same data as in Fig. 1 is used.

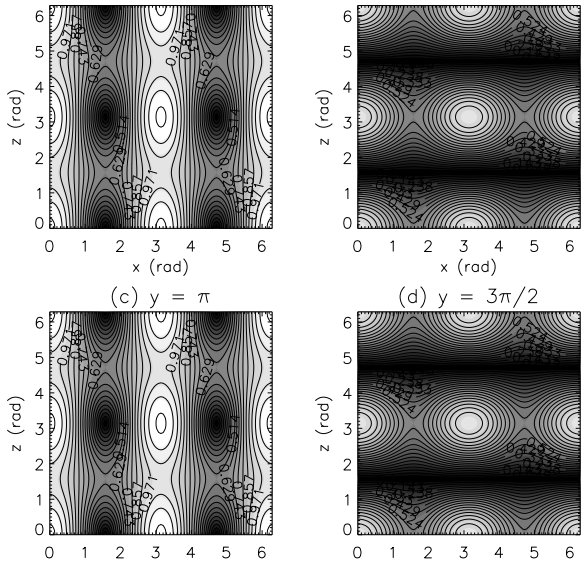

Figure 3. Contour plot of B on (x, z) plane for solution with $A_{111} = l = m = n = 1$. Colour scale: white represents the maximum value 1.15 and black represents zero.

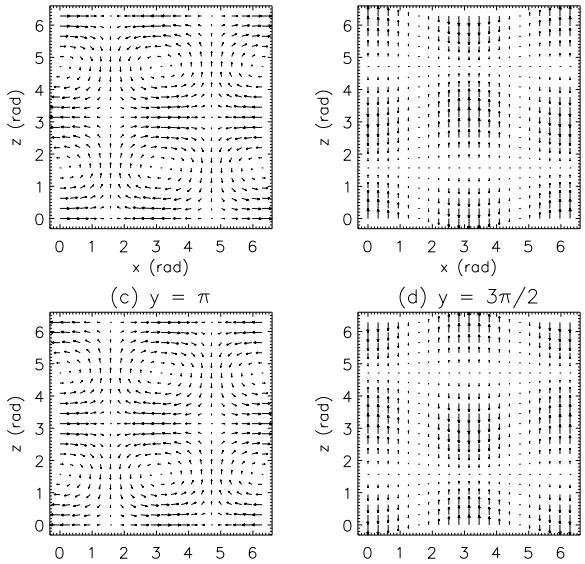

Figure 4. Vector plot of B on (x, z) plane for solution with $A_{111} = l = m = n = 1$. The same data as in Fig. 3 is used.

5. Field configuration near null points

The field line configuration near the null points is obtained by a Taylor expansion of the magnetic field around these points:

$$B_{x_i} = \left.\frac{\partial B_{x_i}}{\partial x_j}\right|_{x_0 y_0 z_0} \delta x_j, \tag{32}$$

where x_i and $x_j \in \{x, y, z\}$, and the null point is represented by (x_0, y_0, z_0). Eq. (32) can be written in matrix form. This allows us to calculate the eigenvalues λ_i with their corresponding eigenvectors $\mathbf{X}_i$, which leads directly to the result $\mathbf{X}_i(s) = \mathbf{X}_i(0)\exp(\lambda_i s)$, where $i = 1, 2, 3$. Field lines with characteristic exponents $\lambda_i < 0$ move towards the null point, and those with $\lambda_i > 0$ move away from the null point. No movement occurs when $\lambda_i = 0$. The system is then in a metastable equilibrium. Due to the divergence free condition, $\sum_{i=1}^{3} \lambda_i = 0$, it follows that all divergence free fields are inherently unstable.

The coordinates of the null points that do not lie on the null lines, are given by (23) or (27). The eigenvalues obtained from their Taylor expansion are presented in Table I, with the integers $i, j, h \in \{0, 1, 2...\}$ corresponding to those in coordinates (27). Using the terminology of Priest and Titov (1996), a spine forms in the x direction and a fan on the (y, z) plane, when $m = n$. One example of this is drawn in Fig. 5.

Next we consider the field around the null points that lie on the null lines. They are given by Eqs. (24) and (25), and can be written explicitly as

$$\left[\ \frac{(2i+1)\pi}{2l}\ ;\ \frac{(2j+1)\pi}{2m}\ ;\ \frac{(2h+1)\pi}{2n}\ \right], \tag{33}$$

$$\left[\ \frac{\pi i}{l}\ ;\ \frac{(2j+1)\pi}{2m}\ ;\ \frac{(2h+1)\pi}{2n}\ \right], \tag{34}$$

where $i, j, h \in \{0, 1, 2, ...\}$. For these null points, the field lines lie on a plane perpendicular to the null line, examples of which are shown in Figs. 6 and 7. The fact that there is no movement in the Ox direction can be seen from Table I, which shows that in both cases the eigenvalue $\lambda_1 = 0$. As before, the integers i, j, h in Table I corresponds to those with coordinates (34), so that the configuration of the field lines changes as the coordinates change.

Table I. Eigenvalues and the basis for each corresponding eigenspace.

Null point	Eigenvalue	Basis of eigenspace
Coordinates (27)	$\lambda_1 = -(-1)^i(-1)^j(-1)^h A_{lmn} l(m^2+n^2)/k$	
		$[1,0,0]$ for $l \neq 0$
	$\lambda_2 = (-1)^i(-1)^j(-1)^h A_{lmn} lm^2/k$	
		$[0,1,0]$ for $l \neq 0$; $m \neq n$
		$[0,1,0]$ and $[0,0,1]$ for $l \neq 0$; $m = n$
	$\lambda_3 = (-1)^i(-1)^j(-1)^h A_{lmn} ln^2/k$	
		$[0,0,1]$ for $l \neq 0$; $m \neq n$
		$[0,1,0]$ and $[0,0,1]$ for $l \neq 0$; $m = n$
Coordinates (33)	$\lambda_1 = 0$	$[1,0,0]$ for $lmn \neq 0$
	$\lambda_2 = A_{lmn} lmn/k$	$[0,1,-(-1)^i(-1)^j(-1)^h]$ for $lmn \neq 0$
	$\lambda_3 = -A_{lmn} lmn/k$	$[0,1,(-1)^i(-1)^j(-1)^h]$ for $lmn \neq 0$
Coordinates (34)	$\lambda_1 = 0$	$[1,0,0]$ for $mn \neq 0$
	$\lambda_2 = A_{lmn} mn(-1)^i(-1)^j(-1)^h$	
		$[0,1,0]$ for $mn \neq 0$
	$\lambda_3 = -A_{lmn} mn(-1)^i(-1)^j(-1)^h$	
		$[0,0,1]$ for $mn \neq 0$

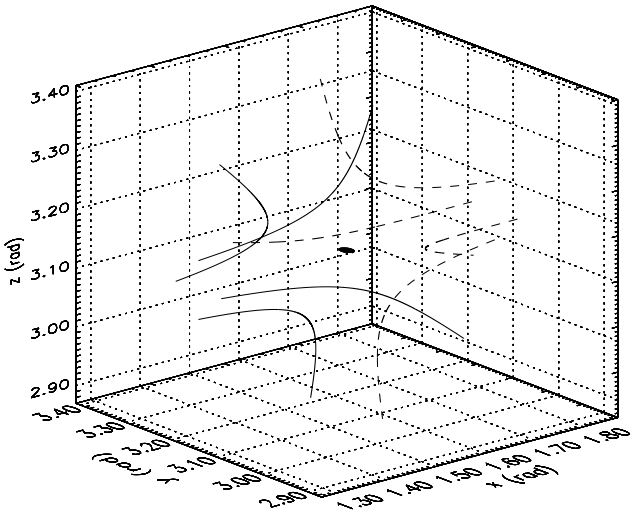

Figure 5. The B field lines for a solution with $A_{111} = l = m = n = 1$, around the null point $[\pi/2, \pi, \pi]$. This is an example of coordinates (27) with $i = 0$, $j = h = 1$. Solid lines represent field lines moving in the positive x direction, and dashed lines move in the negative x direction. The null point is represented by the black dot. The spine is in the x direction and the fan on the (y, z) plane.

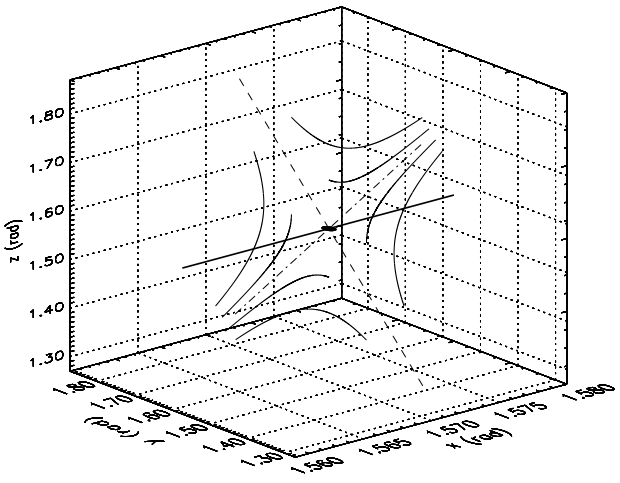

Figure 6. The B field lines for a solution with $A_{111} = l = m = n = 1$, around the null point $[\pi/2, \pi/2, \pi/2]$. This is an example of coordinates (33) with $i = j = h = 0$. The null point lies on a null line, both of which are drawn in bold. The solid lines represent field lines. They move along the dash-dotted line towards the null point and then along the dashed line away from the null point. There is no movement in the x direction, so that every field line lies on a (y, z) plane perpendicular to the null line.

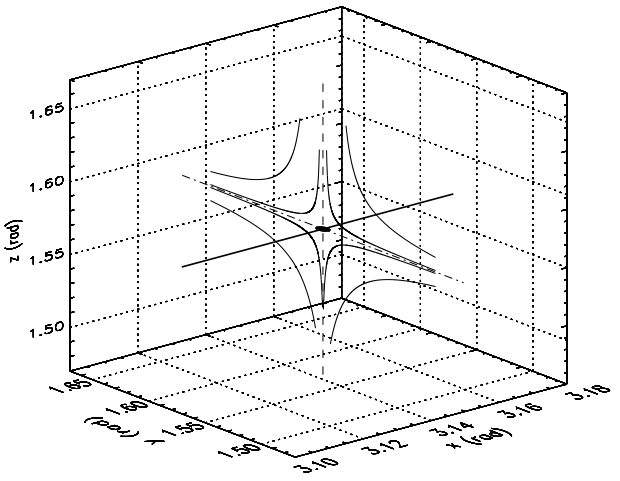

Figure 7. The B field lines for a solution with $A_{111} = l = m = n = 1$, around the null point $[\pi, \pi/2, \pi/2]$. This is an example of coordinates (34) with $i = 1$ and $j = h = 0$. The field configuration is similar to Fig. 6, but rotated by $\pi/4$ around the null line.

6. Field configuration between null points

In order to discuss the field structure between the null points, we simplify the magnetic field by choosing one term (namely $A_{111} = l = m = n = 1$) from the general solution (4) to (6). This allows us to make a comparison with the previous figures in this paper.

From the previous section it is clear that the field structure around the null points is repeated throughout the three-dimensional (3D) space, but with the field orientation changing as one moves from null point to null point. The magnetic field can be thought of as consisting of a limited number of units. These units are fitted together (using rotations, translations, and reflections) to fill the 3D space. One can also see this in Figs. 1 to 4. In this section we will consider only two field structures between the null points, in order to demonstrate the complicated nature of the field lines in 3D space.

Fig. 8 shows the field structure between two null points of the type presented in Fig. 5. The field line forming the spine between the two null points is drawn as a dashed line. The field lines close to the spine rotate in a clockwise direction as they move in the negative Ox direction. This structure is repeated around all the spines in the 3D space, but the rotation alternates between clockwise and anti-clockwise, as can be seen in Fig. 2.

Fig. 9 also shows the field structure between two null points of the type in Fig. 5, but this time we consider the field close to the fan plane. The projection onto the (x, z) plane shows that the field lines do not cross the fan plane, while the (y, z) projection shows that the field lines are not symmetric around the field line joining the two null points. The fact that there is a field component in the negative Oy direction can also be seen in Fig. 2, when one compares the field lines at $y = \pi$ and $z \in (\pi, 2\pi)$ while moving from $x = 0$ to $x = \pi/2$.

7. Stability analysis

The nonlinear behaviour of solution (4) to (6) is studied by considering only one term in its summation series, i.e. only one set of l, m, and n values. A study of the Poincaré plots shows that the field lines are non-ergodic when the constant A_{lmn} in front of the terms, as well as the constants l, m, and n in the arguments of the trigonometric functions, are all integers. Figs. 10 and 11 show the Poincaré plots for $y_c = 3.4$ as the field lines cross it in the positive Oy direction (Fig. 10) and in the negative direction (Fig. 11). These plots are symmetrical around the

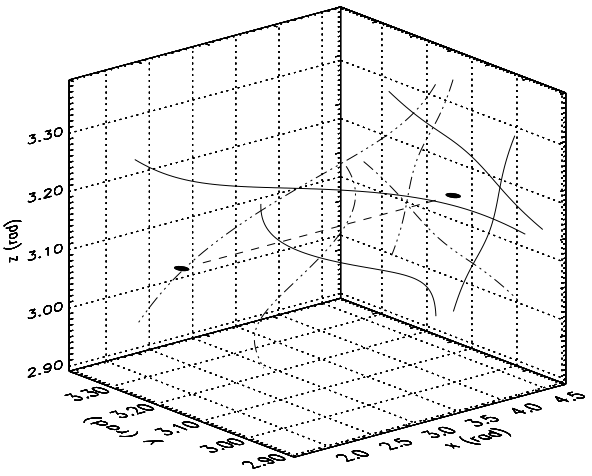

Figure 8. Field lines with $A_{111} = l = m = n = 1$, between null points $(3\pi/2, \pi, \pi)$ and $(\pi/2, \pi, \pi)$. The dashed line is the spine between the null points, which are drawn as black dots. Field lines move in the negative Ox direction, with solid lines representing increasing z values and dot-dashed lines decreasing z values. The projection on the (y, z) plane is added to show the clockwise rotation around the spine.

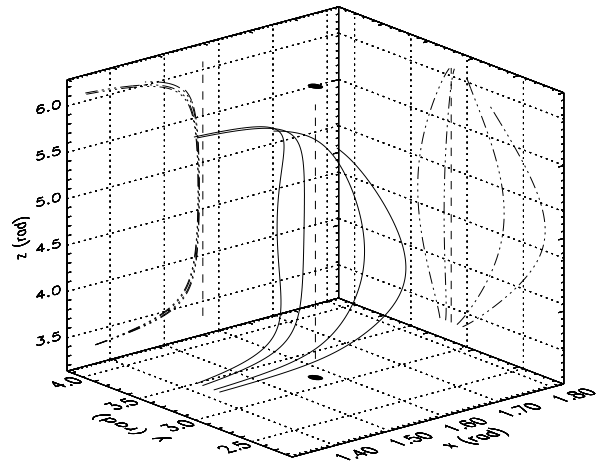

Figure 9. Field lines with $A_{111} = l = m = n = 1$, between null points $(\pi/2, \pi, \pi)$ and $(\pi/2, \pi, 2\pi)$. The dashed line connects the null points (black dots) on the fan plane. Field lines move in the positive Oz direction and are drawn as solid lines. Their (x, z) and (y, z) projections are drawn as dot-dashed lines.

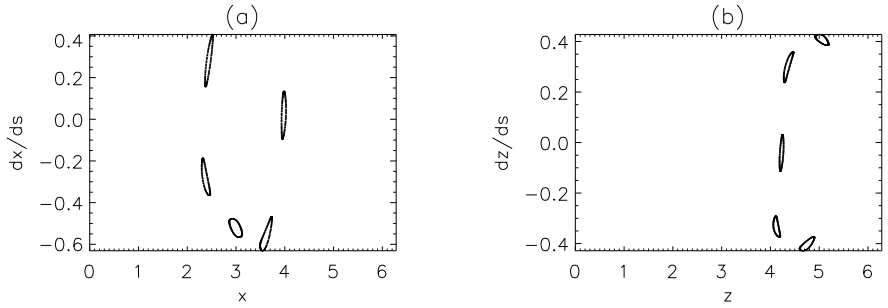

Figure 10. Poincaré plots (a) $(x, \dot{x})$ and (b) $(z, \dot{z})$, taken as the field lines cross $y_c = 3.4$ in the positive Oy direction. The parameters are $A_{111} = l = m = n = 1$ and the initial values are $x_0 = 3.2$, $y_0 = 2.4$, and $z_0 = 3.7$. Each plot contains 1 000 points.

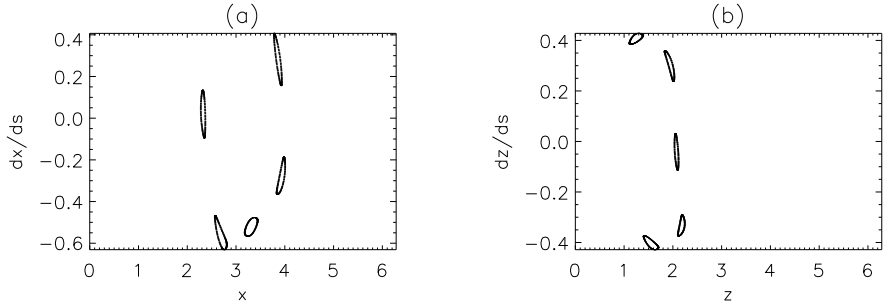

Figure 11. Poincaré plots (a) $(x, \dot{x})$ and (b) $(z, \dot{z})$, taken as the field lines cross $y_c = 3.4$ in the negative Oy direction. The parameters and initial values are the same as in Fig. 10. Each plot contains 1 000 points.

$x = z = \pi$ axes. A similar picture emerges when the Poincaré plots for $z_c = 2.7$ are considered, namely that they are symmetrical around the $x = y = \pi$ axes when the direction in which the field lines cross the z planes changes from positive to negative. For the initial x_0, y_0, and z_0 values used in Figs. 10 and 11, the field lines never cross the plane $x_c = 5.1$. This implies that some field lines do not fill the whole of the three-dimensional space, which corroborates Fig. 9 that shows no field lines crossing the fan plane between two null points.

The symmetries between Poincaré plots depend on the initial values x_0, y_0, and z_0, as well as the choice of x_c, y_c, and z_c planes. Table II shows the relations between different Poincaré plots. Note that one obtains symmetries between the $y_c = 0.25$ and $z_c = 0.25$ planes.

Poincaré plots with non-integer A_{lmn} values show no sign of chaotic behaviour. The reason for this is that each term in the solution is

Table II. Symmetries between Poincaré plots with $x_0 = y_0 = z_0 = 1.0$, for field lines crossing planes $x_c = y_c = z_c = 0.25$. Parameters $A_{111} = l = m = n = 1$ were used.

Poincaré plot	Reflection axis	Poincaré plot
$(y, \dot{y})$ cross x_c in $-Ox$ direction	$y = \pi$	$(y, \dot{y})$ cross x_c in $+Ox$ direction
$(z, \dot{z})$ cross x_c in $-Ox$ direction	$z = \pi$	$(z, \dot{z})$ cross x_c in $+Ox$ direction
$(x, \dot{x})$ cross y_c in $+Oy$ direction	$x = \pi$	$(x, \dot{x})$ cross z_c in $-Oz$ direction
$(x, \dot{x})$ cross y_c in $-Oy$ direction	$x = \pi$	$(x, \dot{x})$ cross z_c in $+Oz$ direction
$(y, \dot{y})$ cross z_c in $-Oz$ direction	$\dot{y} = \dot{z} = 0$	$(z, \dot{z})$ cross y_c in $+Oy$ direction
$(y, \dot{y})$ cross z_c in $+Oz$ direction	$\dot{y} = \dot{z} = 0$	$(z, \dot{z})$ cross y_c in $-Oy$ direction

multiplied by A_{lmn}, so that the whole solution simply scales with A_{lmn}. An example of a non-integer value of l is presented in Fig. 12. We found that for non-integer l values the solution does not show ergodic behaviour. Not only that, but movement along the Ox direction seems to be severely restricted. However, non-integer values of m and n leads to ergodic behaviour. Figs. 13 to 15 present the case for $m = 3.731$, and for non-integer n values we obtain similar Poincaré plots. The reason for the difference between non-integer l values versus non-integer m and n values, is not obvious. It is likely that the relative sizes between the terms in the solution play a role. With this in mind, it is interesting

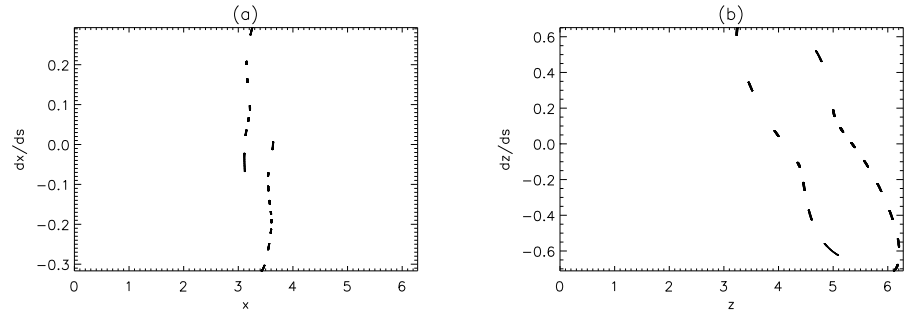

Figure 12. Poincaré plots (a) $(x, \dot{x})$ and (b) $(z, \dot{z})$, taken as the field lines cross $y_c = 4$ in the negative Oy direction. The parameters are $A_{l11} = m = n = 1$, $l = 3.731$ and the initial values are $x_0 = 3.1$, $y_0 = 1.9$, and $z_0 = 5.5$. The number of points in each plot is 1 839.

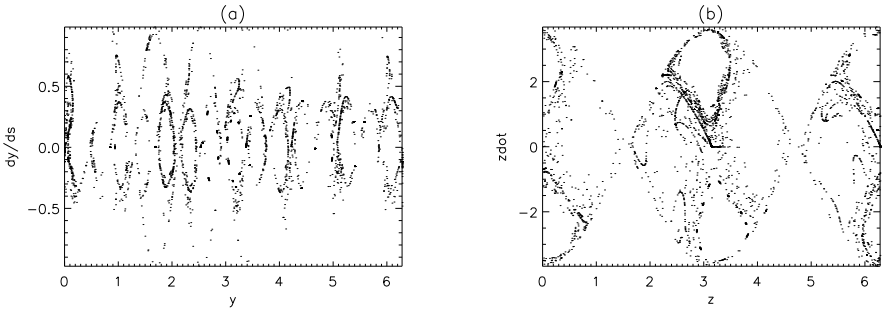

Figure 13. Poincaré plots (a) $(y, \dot{y})$ and (b) $(z, \dot{z})$, taken as the field lines cross $x_c = 3$ in the positive Ox direction. The parameters are $A_{1m1} = l = n = 1$, $m = 3.731$ and the initial values are $x_0 = 3.1$, $y_0 = 1.9$, and $z_0 = 5.5$. The number of points in each plot is 4 000.

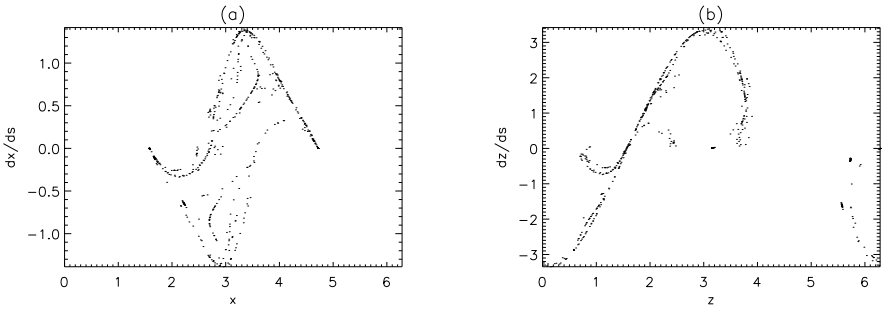

Figure 14. Poincaré plots (a) $(x, \dot{x})$ and (b) $(z, \dot{z})$, taken as the field lines cross $y_c = 2$ in the positive Oy direction. The parameters and initial values are the same as in Fig. 13. The number of points in each plot is 636.

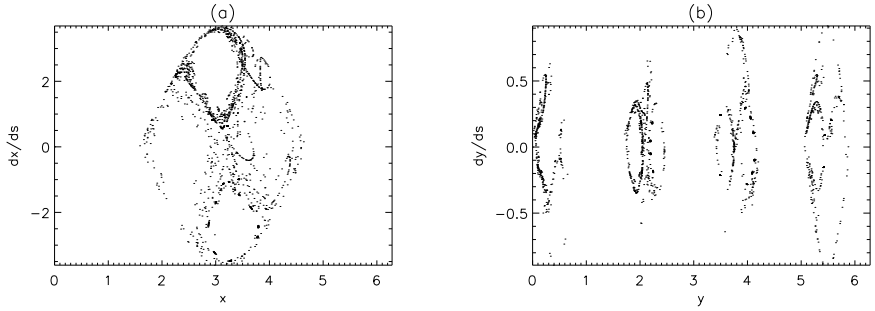

Figure 15. Poincaré plots (a) $(x, \dot{x})$ and (b) $(y, \dot{y})$, taken as the field lines cross $z_c = 3$ in the positive Oz direction. The parameters and initial values are the same as in Fig. 13. The number of points in each plot is 2 068.

to observe that for large chosen values of l, Eq. (4), the x component of the solution, becomes much smaller than the y and z components, Eqs. (5) and (6). For a large m value, the y component is much smaller than the x and total z component, while the z component consists of a large first term and a small second term. A similar picture emerges for large n values.

By making the identification $\dot{x_i} = B_{x_i}$ with $x_i \in \{x, y, z\}$, as in Eq. (7), we are able to draw the phase plots $(\dot{x_i}, x_i)$. Fig. 16 is obtained by projecting the values of B_x from three-dimensional space onto the x axis, i.e. by drawing B_x along the x axis for all values of y and z. It shows the position of the null points at $x \in \{\pi/2, 3\pi/2\}$, as well as $\max(B_x) = 1.15$ at $x \in \{0, \pi, 2\pi\}$. The null lines are parallel to the x axis and do not show in Fig. 16. One cannot assign any direction to the field lines, because the projection overlays different lines. As an example, the null point at $x = \pi/2$ has field lines pointing towards it in the Ox direction at $y = 0,\ z = 0$, but away from it at $y = 0,\ z = \pi$, as can be seen in Fig. 4. Similarly, the phase plot $(\dot{y}, y)$ in Fig. 17 is a projection of the values of B_y from three dimensions onto the y axis. The null points are located at $y \in \{0, \pi, 2\pi\}$, and the null lines at $y \in \{\pi/2, 3\pi/2\}$. The amplitude of the field is easily observed in Figs. 16 and 17. Fig. 16 shows that the x dependence of B_x takes the form $1.15\cos(x)$, corresponding to Eq. (4). From Eq. (5) we know that the y dependence of B_y consists of a combination of sine and cosine terms. Fig. 17 shows that the contribution from its $\sin(y)$ component is 0.58 that from its $\cos(y)$ component. The projection of B_z onto the z axis gives an identical picture to Fig. 17.

8. Conclusion

The classic solution by Arnold of the force free field equation revealed the existence of null points in ordinary flows and magnetic fields. The same paper proved the chaotic nature of such configurations and showed the rich structure of this sub-Eulerian flow. Up till now it has been the only known constant α field in three dimensional Cartesian space, apart from trivial permutations, translations and rotations, and a considerable amount of research has been dedicated to the study of its implications for solar magnetic configurations, as well as for controlled fusion laboratory devices. By comparison, not much information is available on ordinary flows with regard to turbulence.

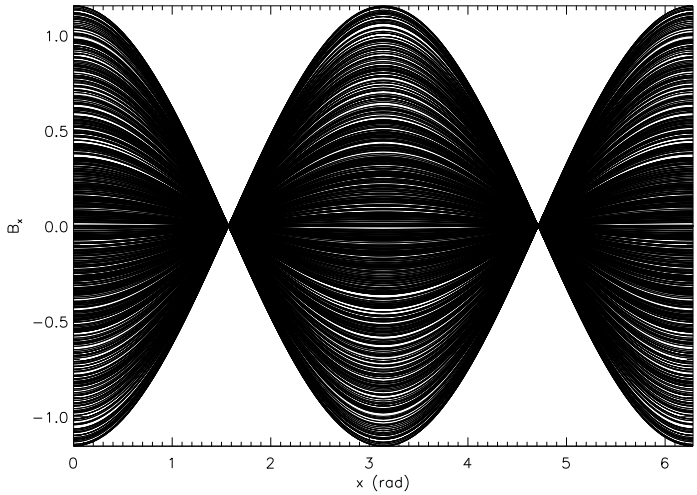

Figure 16. The phase plot $(\dot{x}, x)$ with parameters $A_{111} = l = m = n = 1$. The plot is obtained by projecting the values of B_x onto the x axis.

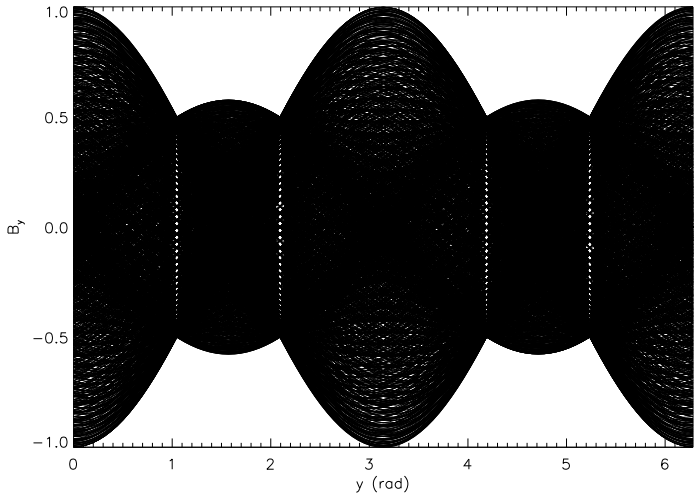

Figure 17. The phase plot $(\dot{y}, y)$ with parameters $A_{111} = l = m = n = 1$. It is obtained by projecting the B_y values onto the y axis. The plot $(\dot{z}, z)$ is identical to this.

We have presented here a new set of solutions for linear force free fields, that is independent of Arnold's solution. This new family of solutions admits sets of null points and bundles of null lines. The existence of the integral of energy, which was constructed analytically, shows the existence of hyper-tori in phase space, on which these sets of points lie.

All this information points to the existence of an extremely complex substructure underlying the Eulerian flows. The implications for the generation of turbulence, magnetic and hydrodynamic alike, remain to be explored.

Acknowledgements

We would like to thank the anonymous referee for suggesting the integral representation with the Dirac-delta function, as well as general remarks which has improved the presentation of this paper.

References

Arnold, V. I.: 1965, 'Sur la topologie des écoulements stationnaires des fluides parfaits'. *Comptes Rendues de l'Académie des Sciences, Paris* **261**, 17–20.

Berton, R.: 2000, 'Consistent determination of quasi force-free magnetic fields from observations in solar active regions'. *Astronomy and Astrophysics* **356**, 301–7.

Biskamp, D.: 1993, *Nonlinear Magnetohydrodynamics*, Vol. 1 of *Cambridge Monographs on Plasma Physics*. CUP, Cambridge.

Bungey, T. N., V. S. Titov, and E. R. Priest: 1996, 'Basic topological elements of coronal magnetic fields'. *Astronomy and Astrophysics* **308**, 233–47.

Clegg, J. R., P. K. Browning, P. Laurence, B. J. I. Bromage, and E. Stredulinsky: 2000, 'The linear force-free field in a spherical shell using a new method to determine the coefficients of the eigenfunction expansion'. *Astronomy and Astrophysics* **361**, 743–58.

Démoulin, P., L. G. Bagalá, C. H. Mandrini, J. C. Hénoux, and M. G. Rovira: 1997, 'Quasi-separatrix layers in solar flares II. Observed magnetic configurations'. *Astronomy and Astrophysics* **325**, 305–17.

Dombre, T., U. Frisch, J. M. Greene, M. Hénon, A. Mehr, and A. M. Soward: 1986, 'Chaotic streamlines in the ABC flows'. *Journal of Fluid Mechanics* **167**, 353–91.

Evangelidis, E. A., L. L. Vaughan, and G. J. J. Botha: 2000, 'The structure of force-free magnetic fields'. *Solar Physics* **193**(1-2), 17–32.

Galsgaard, K. and Å. Nordlund: 1997, 'Heating and activity of the solar corona 3. Dynamics of a low beta plasma with three-dimensional null points'. *Journal of Geophysical Research* **102**(A1), 231–48.

Galsgaard, K., E. R. Priest, and Å. Nordlund: 2000, 'Three-dimensional separator reconnection – How does it occur?'. *Solar Physics* **193**(1-2), 1–16.

Hénon, M.: 1966, 'Sur la topologie des lignes de courant dans un cas particulier'. *Comptes Rendues de l'Académie des Sciences, Paris* **262**, 312–4.

Marsh, G. E.: 1996, *Force-Free Magnetic Fields. Solutions, Topology and Applications*. World Scientific, Singapore.

Moon, Y.-J., G. S. Choe, H. S. Yun, Y. D. Park, and D. L. Mickey: 2002, 'Force-freeness of solar magnetic fields in the photosphere'. *The Astrophysical Journal* **568**, 422–31.

Priest, E. R. and V. S. Titov: 1996, 'Magnetic reconnection at three-dimensional null points'. *Philosophical Transactions: Mathematical, Physical and Engineering Sciences* **354**(1721), 2951–92.

Yurchyshyn, V. B., H. Wang, J. Qiu, P. R. Goode, and V. I. Abramenko: 2000, 'Magnetic topology in 1998 November 5 two-ribbon flare as inferred from ground-based observations and linear force-free modelling'. *The Astrophysical Journal* **540**, 1143–9.